ADVANCED HEALTHCARE MATERIALS
www.advhealthmat.de

Enhanced Antigen Capture via Cholinephosphate-Mediated Cell Membrane Interactions to Improve In Situ Tumor Vaccines

Ting Song, Xin Cui, Jiansheng Lin, Zonghua Liu, Linghong Huang,* and Wei Xue**

Inadequate antigen capture and insufficient antigen-presenting cell (APC) activity at tumor sites limit the effectiveness of in situ vaccines. To address this, poly(glutamic acid-cholinephosphate) (pGluCP) is introduced as a polymer with cell membrane adhesion properties capable of capturing both water-soluble and insoluble membrane antigens from necrotic tumor cells while recruiting more APCs. The approach uses manganese-mineralized black phosphorus (MnBP) coated with pGluCP and αPD-1 antibodies to create the MnBP@pGluCP-αPD-1 complex for in situ vaccines. MnBP eradicates tumor cells via photothermal effects, releasing antigens, while Mn^{2+} ions activate the intracellular STING pathway, acting as an adjuvant. pGluCP captures these antigens, forming pathogen-mimicking micro-nanoparticles, leading to an in situ vaccine (MnBP@pGluCP/antigens) that co-localizes antigens and adjuvants. The αPD-1 antibody alleviates tumor-induced immune suppression, enhancing tumor cell-specific killing. This study demonstrates the potential of leveraging cholinephosphate-cell membrane interactions to improve antigen presentation efficiency, significantly bolstering the efficacy of in situ tumor vaccines and opening new avenues for advanced cancer immunotherapy.

1. Introduction

In recent years, tumor immunotherapy has emerged as a transformative force in clinical oncology, becoming a focal point for innovative cancer treatments.[1,2] Among the various strategies, in situ tumor vaccines have garnered significant attention due to their ability to harness the body's immune system against existing tumors. These vaccines operate by inducing localized tumor cell death, releasing tumor antigens, which are then captured and presented by antigen-presenting cells (APCs). This process initiates a cascade of immune responses, tailored specifically to combat the patient's tumor, offering personalized therapy that is simple, time-efficient, economical, and universally applicable with minimal side effects.[3,4] Despite their potential, in situ tumor vaccines often fall short in eliciting robust immune responses necessary to eradicate tumors. This limitation stems from the complexity of the immune response cascade, particularly the inefficiency of APC-mediated tumor antigen presentation, which acts as a critical bottleneck.[5]

Recent advancements have focused on the importance of enhancing tumor antigen capture and presentation. Functional nanocarriers, equipped with protein adsorption groups like amino groups, have been designed to bind to and transport tumor antigens to lymph nodes (LNs), thereby improving antigen presentation.[6–11] Hydrogel-based 3D networks have also been proposed as effective antigen traps that can retain and concentrate antigens at the site of injection, facilitating their uptake by APCs.[12,13] It is noteworthy that capturing both water-soluble and water-insoluble tumor antigens to mimic pathogen-like particles significantly boosts antigen presentation efficiency.[14] However, capturing water-insoluble tumor cell membrane antigens presents a significant challenge. These antigens, often embedded within the liquid bilayer of tumor cells, are difficult to extract and transport. Despite the progress made with functional nanocarriers and hydrogel networks, there are currently limited reports of successful strategies for effectively capturing and delivering these challenging antigens. Further research is needed to develop innovative methods for handling water-insoluble tumor cell membrane antigens, which could significantly enhance the efficacy of cancer immunotherapies.

This study introduces poly(glutamic acid-cholinephosphate) (pGluCP), a cell membrane-adhesive polymer capable of capturing water-soluble protein antigens and water-insoluble membrane antigens released upon tumor cell death. pGluCP's unique ability to attract dendritic cells (DCs) via membrane adsorption facilitates the internalization of tumor antigens.

T. Song, X. Cui, Z. Liu, W. Xue
Department of Biomedical Engineering
Jinan University
Guangzhou 510632, China
E-mail: tliuzonghua@jnu.edu.cn; txuew@jnu.edu.cn
J. Lin
Department of Anatomy
Hunan University of Chinese Medicine
Changsha 410208, China
L. Huang
Department of Urology, Guangzhou Institute of Urology, Guangdong Key Laboratory of Urology, The First Affiliated Hospital of Guangzhou Medical University
Guangzhou Medical University
Guangzhou, Guangdong 510230, China
E-mail: 2019991016@gzhmu.edu.cn
The ORCID identification number(s) for the author(s) of this article can be found under https://doi.org/10.1002/adhm.202403460

DOI: 10.1002/adhm.202403460

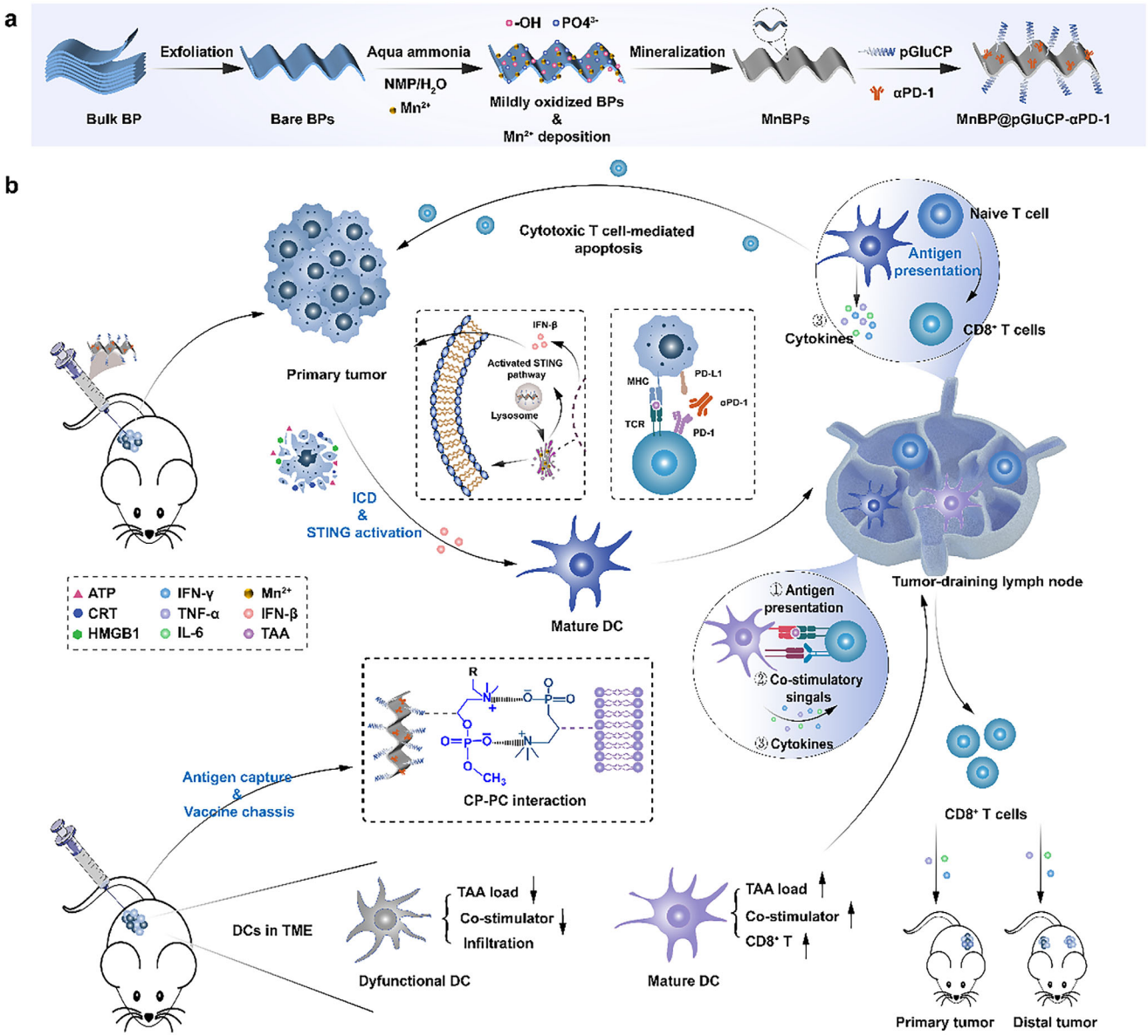

Scheme 1. Schematic illustration of the preparation of antigen-capturing nanoparticles and its principle for immunotherapy. a) The preparation of MnBP@pGluCP-αPD-1. b) Schematic illustration of antigen-capturing nanoparticles based on CP-cell membrane interactions for enhanced antigen capture and DCs recruitment.

Cholinephosphate (CP) groups, designed to mimic phosphatidylcholine (PC) head groups, exhibit strong cell membrane adhesion and have been utilized in various applications, including tissue adhesives and drug delivery systems.[15–24] Our previous work demonstrated pGluCP's potential in binding tumor antigens in vitro to form conventional vaccines.[25]

Herein, we present the synthesis of Mn^{2+}-mineralized black phosphorus (MnBP) coated with pGluCP and αPD-1 antibody to construct an in situ tumor vaccine complex (**Scheme 1**). This approach boasts several advantages: 1) MnBP exhibits a superior photothermal effect, efficiently eliminating tumor cells and triggering immunogenic cell death (ICD), which leads to the release of tumor antigens. Mn^{2+} ions activate the STING pathway, acting as an adjuvant to further enhance the immune response. 2) pGluCP captures both water-soluble and water-insoluble antigens, forming pathogen-like particles that co-localize with the adjuvant, creating an in situ vaccine (MnBP@pGluCP/antigens). 3) The CP-PC interaction provides a robust platform for vaccine assembly and delivery. 4) αPD-1 antibody mitigates tumor-induced T cell suppression by blocking the PD-1/PD-L1 pathway, enhancing tumor cell killing. By leveraging the unique adhesion properties of pGluCP toward tumor cell antigens and APC cell membranes, this strategy holds significant promise for developing novel in situ tumor vaccines that enhance APC antigen presentation efficiency. This innovative approach represents a significant step forward in the quest for more effective cancer immunotherapies.

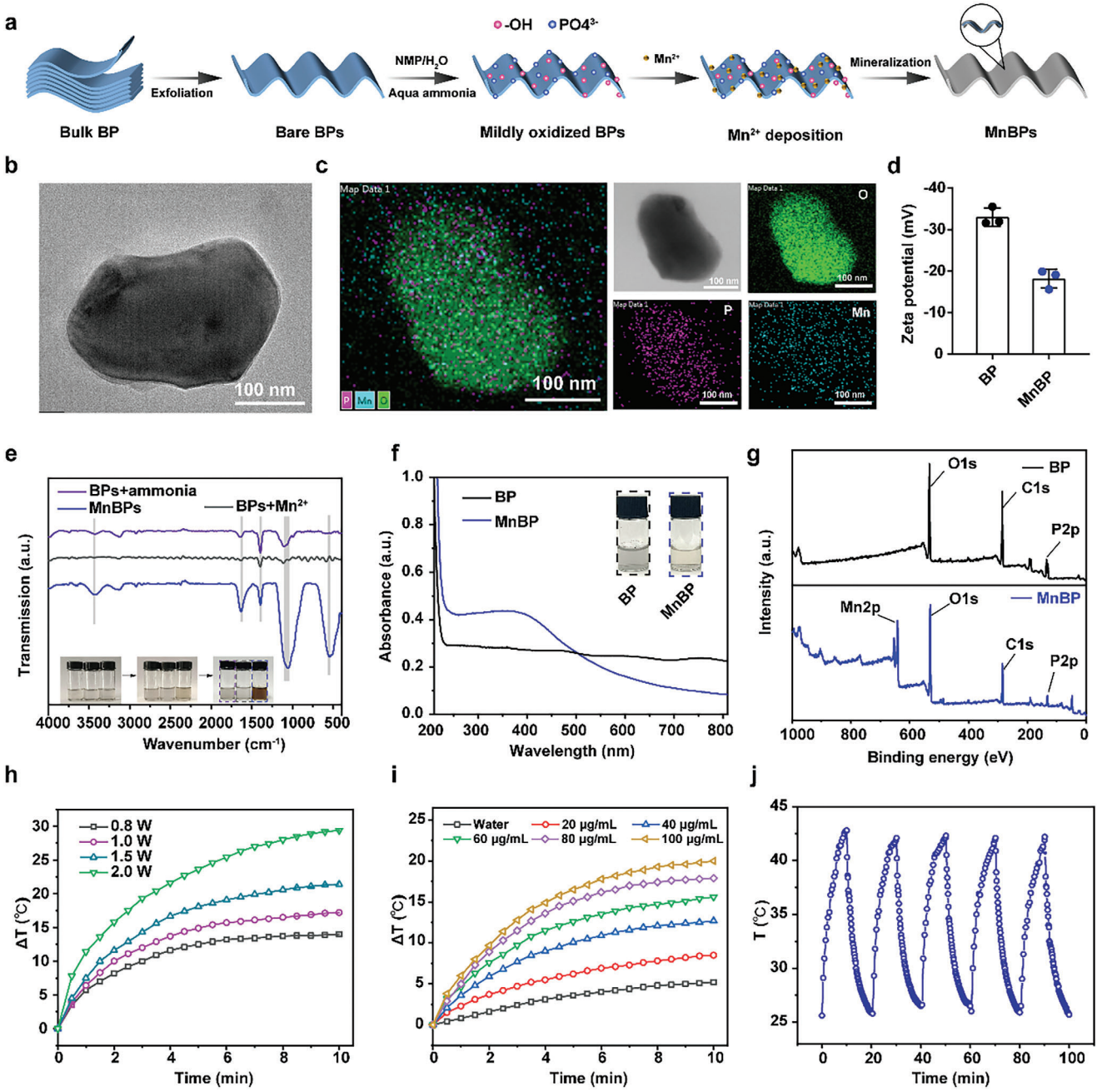

Figure 1. Schematic of MnBP construction and characterization. a) Illustration of the synthesis of MnBPs. b) HRTEM images of MnBP (scale bar = 100 nm). c) Elemental mapping of MnBP (Scale bar = 100 nm). d) Zeta potentials of BP and MnBP. e) FT-IR spectra of BPs+ammonia (without Mn^{2+}), BPs+Mn^{2+} (without ammonia), and MnBPs. e) Photothermal curves of MnBP at different laser power densities. f) UV–vis absorption spectra of BP and MnBP. g) XPS spectra of BP and MnBP. h) Temperature change curves of MnBP after exposure to continuous laser irradiation (808 nm, 1.5 W cm^{-2}, 600 s). i) Temperature change curves of MnBP with different concentrations after exposure to continuous laser irradiation. j) Photothermal stability of MnBP through five cycles of continuous heating/cooling process.

2. Results and Discussion

2.1. Preparation and Characterization of MnBP or MnBP@pGluCP

The preparation of BP nanosheets and their subsequent mineralization with manganese phosphate (MnP) was achieved following established protocols.[26] Initially, BPs were gently oxidized using a solution of N-methyl-2-pyrrolidone (NMP) containing ammonia, which provided a phosphorus source and created reactive sites for Mn^{2+} deposition. The addition of manganese chloride ($MnCl_2$) catalyzed the electrostatic deposition of MnP onto the BP surface (**Figure 1a**). The impact of varying sonication times on the morphology and properties of BPs was

investigated using transmission electron microscopy (TEM) and dynamic light scattering (DLS) for particle size and surface potential analysis. TEM images revealed the successful transformation of bulk BPs into bare BPs through sonication, with a notable decrease in particle size as sonication time increased up to a certain point (Figure S1a, Supporting Information). However, beyond 18 h of sonication, the reduction in particle size and surface potential became negligible (Figure S1b,c, Supporting Information). Among them, the bare BPs sonicated for 18 h exhibited a characteristic lamellar structure, a size of ≈340 nm, and an average surface potential of −31.6 mV, which was selected for further experiments. The X-ray diffraction (XRD) patterns of BP nanosheets showed their diffraction peaks at the (002), (004), and (006) crystal planes (Figure S2, Supporting Information), which match the standard XRD pattern for BPs. Post-MnP deposition, the lamellar morphology of BPs was preserved, as evidenced by TEM (Figure 1b). Energy-dispersive X-ray spectrometry (EDS) mapping confirmed the uniform distribution of phosphorus, manganese, and oxygen on MnBP- surfaces (Figure 1c). After the mineralization of BP by MnP, the zeta potential of BPs increased from −31.9 to −19.1 mV, reflecting the neutralization of phosphate anions by Mn^{2+} (Figure 1d). The chemical composition of MnBP was measured by Fourier transform infrared (FTIR) spectroscopy and X-ray photoelectron spectroscopy (XPS). FTIR spectra displayed broad absorption bands at 509, 547, 1052, and 1394 cm^{-1} attributed to P–O and P = O stretching vibrations. A pronounced absorption band at 3430 cm^{-1} indicated the presence of OH^- stretching, with enhanced intensity and broadening in MnBPs versus the "BPs+ammonia" group, confirming the formation of intermolecular and weak hydrogen-bonded OH in MnP. The absence of OH^- and PO_4^{3-} bands in BPs and BPs+Mn^{2+} (without ammonia) suggested the critical role of aqueous ammonia in the mineralization process, corroborated by changes in the reaction solution (Figure 1e). The UV–vis absorption spectra of BPs and MnBPs showed broad-spectrum absorption, with MnBP exhibiting stronger absorption (Figure 1f). In addition, XPS analysis also showed the presence of Mn in the MnBP (Figure 1g). These results proved that the surface of BPs was successful in mineralization by MnP.

The biologically inspired polyvalent choline phosphate polymer, pGluCP, is a cationic polymer synthesized by "click" chemistry that exhibits unique characteristics in biomaterial design. ^{1}H NMR spectrum of the pGluCP (δ: ppm, 400 MHz, D_2O): 8.43, (s, 1H, dC***H***N_3), 4.69 (s, 2H, –N–C***H***$_2$CN_3), 4.60 (s, 2H, $N_3CH_2CH_2C$***H***$_2$–), 4.41 (br s, 1H, –C***H***NH–), 4.10 (s, 2H, N_3C***H***$_2CH_2$d, 2H, –OC***H***$_3$), 3.16 (6H, –N(C***H***$_3$)$_2$), 2.49 (br s, 2H, –COC***H***$_2CH_2$–), 2.29 (br s, 2H, N_3CCH_2–), 3.92 (m, 2H, –OC***H***$_2CH_2$N–), 3.75 (m, 2H, –OCH_2C***H***$_2$N–), 3.61–3.59 (H_2C***H***$_2CH_2$–), and 2.12–2.00 (br, 2H, –$COCH_2$C***H***$_2$–) was shown (Figure S5, Supporting Information). The ^{13}C NMR spectrum of the pGluCP is shown in Figure S6, Supporting Information. pGluCP exhibited exceptional biocompatibility (Figure S7, Supporting Information). Subsequently, the positively charged pGluCP interacted electrostatically with the negatively charged MnBP to prepare MnBP@pGluCP. The optimal mass ratio of MnBP to pGluCP for effective modification was determined to be 1: 6, as evidenced by the saturation of pGluCP binding (Figure S8, Supporting Information). This optimized ratio was employed for the preparation of MnBP@pGluCP for subsequent studies.

2.2. Photothermal Effect of MnBP or MnBP@pGluCP

A pivotal concern in high-temperature photothermal therapy (PTT), typically exceeding 55 °C under near-infrared light (NIR) irradiation, is the inadvertent damage inflicted upon neighboring healthy tissues and cells.[27] For this reason, we expected to heat the tumor to a slightly higher local temperature of 41–45 °C to achieve good biosafety. To explore the optimal photothermal conditions, first, the MnBP suspensions were subjected to different laser power densities, which showed that 1.5 W cm^{-2} was the ideal condition (Figure 1h). The temperature increase was concentration-dependent during continuous irradiation (Figure 1i). Specifically, at a concentration of 100 µg mL^{-1}, the temperature of the MnBP suspension steadily rose to 43 °C. Notably, the solution retained its heating capacity to a comparable level across five consecutive laser switching cycles, underscoring the outstanding photothermal stability of MnBP (Figure 1j). Collectively, these results indicate that continuous irradiation of 100 µg mL^{-1} MnBP suspensions at 1.5 W cm^{-2} for 3 min is sufficient to accomplish mild thermotherapy objectives. Importantly, the MnBPs retained exceptional photothermal conversion capability and photothermal stability throughout the study.

2.3. ICD Induced by Photothermal Therapy

Emerging evidence suggests that PTT can significantly overcome the challenge of low immune responses within the tumor microenvironment (TME) by stimulating the immune system through the liberation of tumor-associated antigens (TAAs) and danger-associated molecular patterns (DAMPs).[28–31] Key DAMPs include high-mobility group box 1 (HMGB1), ATP, and calreticulin (CRT), which play pivotal roles in enhancing the immune response. Specifically, HMGB1 facilitates the delivery of optimal antigens to T cells, ATP attracts APCs to the tumor site, and CRT notably amplifies the phagocytosis of apoptotic cells and cellular debris.[32,33] First, the viability of 4T1 cells was assessed following PTT. The photothermal conversion capabilities of MnBP and MnBP@pGluCP were verified by an infrared photothermal imager (**Figure 2a**). The results illustrated that the apoptosis rate of 4T1 cells induced by PTT using MnBP@pGluCP was 46.38%, whereas PTT mediated by MnBP alone resulted in an apoptosis rate of 23.47%. This discrepancy highlights that the surface modification of pGluCP on MnBP markedly boosts tumor cell-killing efficiency (Figure 2b). Additionally, as shown in Figure 2c, prominent ATP expression was observed in the MnBP+L-containing groups, and the ATP expression in the MnBP@pGluCP+L group was significantly higher than that in the MnBP+L group. Furthermore, the MnBP@pGluCP+L group displayed the highest levels of CRT exposure and HMGB1 release, as quantified by enzyme-linked immunosorbent assay (ELISA). These findings demonstrated that PTT using the MnBP-based platform not only effectively eradicates 4T1 tumor cells but also triggers the release of DAMPs. Notably, the MnBP@pGluCP group showed substantially increased CRT exposure, HMGB1, and ATP secretion. This enhanced effect is attributed to the pGluCP component, which efficiently binds to tumor cell membranes, promotes interactions between MnBPs

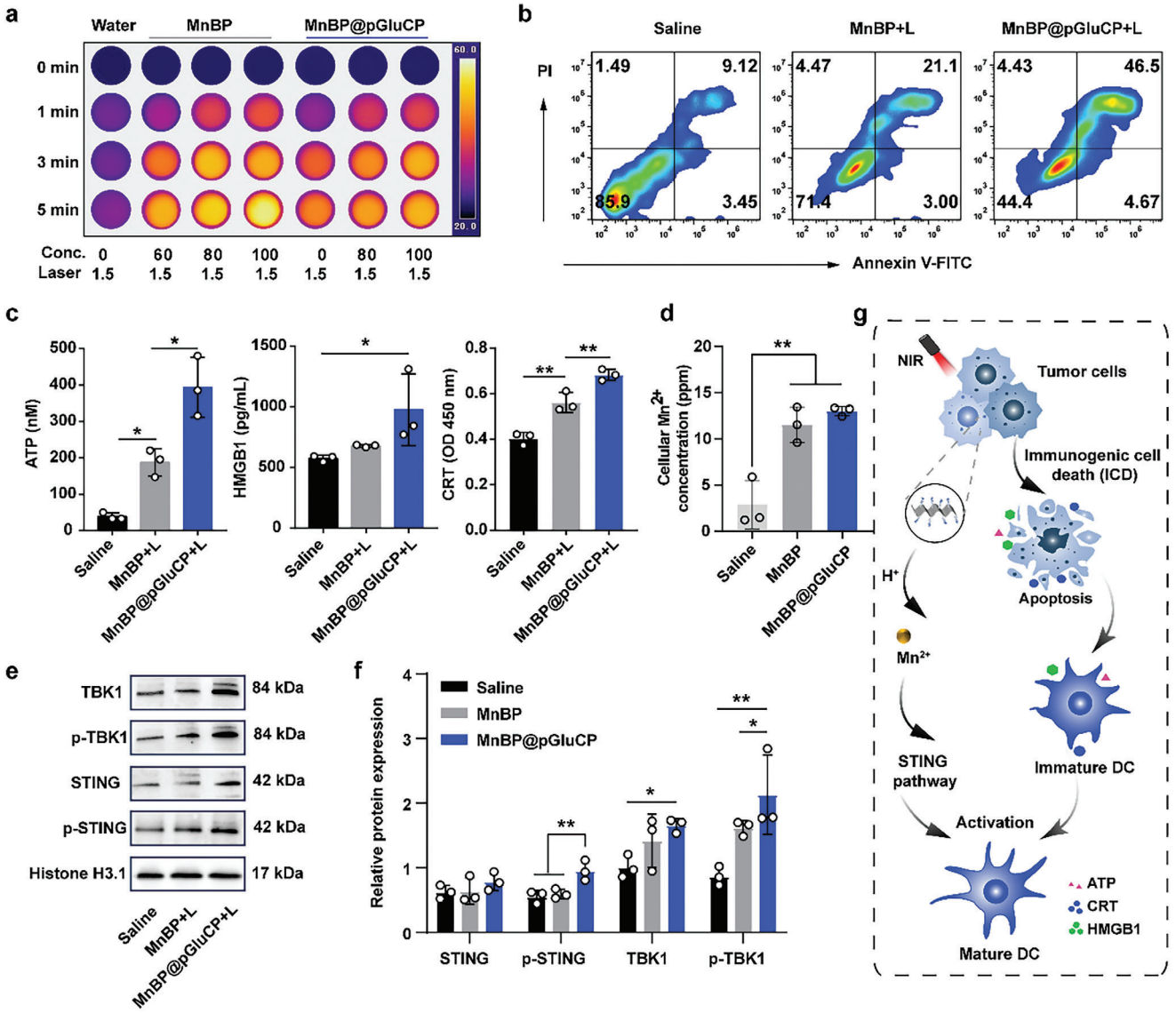

Figure 2. Antigen release and STING pathway activation. a) Infrared thermal imaging of MnBP and MnBP@pGluCP with laser irradiation (808 nm, 1.5 W cm^{-2}). b) Apoptosis of 4T1 cells treated with 808 nm laser. c) Detection of ATP, HMGB1 and CRT release after different treatments ($n = 3$). d) Cellular Mn^{2+} concentration. e) Representative Western blotting images showing the expression of TBK1, p-TBK1, STING, and p-STING. f) Quantification of TBK1, p-TBK1, STING, and p-STING levels relative to their respective total proteins and normalized to Histone H3.1. c) Schematic illustration of the mechanism underlying photothermal-induced ICD and subsequent STING pathway activation leading to DC maturation. All data are presented as mean ± SD ($n = 3$). *$p < 0.05$, and **$p < 0.01$.

and tumor cells, and thereby amplifies the photothermal therapeutic outcome.

2.4. Activation of the STING Pathway

The release of Mn^{2+} was initially detected, as depicted in Figure 2d, inductively coupled plasma mass spectrometry (ICP-MS) analysis revealed a significant increase in intracellular Mn^{2+} release in both the MnBP and MnBP@pGluCP groups compared to the control. This increase is crucial for initiating the cGAS-STING cascade in DCs, which plays a pivotal role in activating innate immunity and mounting an antitumor response. Subsequently, the expression levels of STING and TBK1 were analyzed by Western blotting to further investigate the activation of this signaling pathway. The results, presented in Figure 2e, confirmed the upregulation of STING and TBK1 following MnBP@pGluCP treatment, supporting the notion that Mn^{2+} are potent activators of the STING pathway. These findings are consistent with previous studies demonstrating the involvement of Mn^{2+} in innate immune signaling pathways. As shown in Figure 2f, the phosphorylation levels of TBK1 and STING were moderately increased after MnBP treatment compared with the control group, and the expression of TBK1 and STING

as well as their phosphorylation levels were also significantly increased by MnBP@pGluCP treatment. These findings suggest that MnBP@pGluCP effectively activates the STING pathway, promoting the phosphorylation and subsequent activation of STING and TBK1 through direct or indirect mechanisms.

As depicted in Figure 2g, a robust strategy for inducing DC maturation is based on the induction of immunogenic cell death by PTT and the subsequent activation of the STING pathway. This approach underscores key findings regarding the liberation of DAMPs, the enhanced efficacy of MnBP@pGluCP in inducing cell death, and the activation of the STING pathway by Mn^{2+}.

2.5. Antigen Capture and Enhanced Presentation by MnBP@pGluCP Through Simultaneous Capture

PC, a predominant component of mammalian cell membranes, undergoes orientation isomerization to form CP. This transformation facilitates electrostatic interactions between the choline phosphate groups in the pGluCP polymer and the phosphatidylcholine components of cell membranes (**Figure 3a**). Cell lysates contain a wide array of intracellular components, including both water-soluble and water-insoluble antigens. Confirmation of this antigen capture was achieved through sodium dodecyl sulfate-polyacrylamide gel electrophoresis (SDS-PAGE), which revealed a richer protein profile in the lysates captured by MnBP@pGluCP compared to those captured by MnBP (Figure 3b). To quantify the antigen-capturing capacity of MnBP@pGluCP, different particles were co-incubated with cell lysates, and the protein concentration was measured using a BCA kit at various time points. As shown in Figure 3c, MnBP@pGluCP demonstrated a rapid and efficient capture of 4T1 cell lysates, with the total amount of protein captured being ≈1.8 times higher than that captured by MnBP alone. This significant enhancement in capture ability has led to a notable change in the zeta potential of MnBP@pGluCP from positive to negative (Figure 3d). This shift suggests that MnBP@pGluCP has the potential to capture a greater number and variety of antigens, which could be beneficial for its application in immunotherapeutic strategies.

Given the minimal protein capture by MnBP, the pGluCP component appears to be the primary driver behind the exceptional protein capture ability of MnBP@pGluCP. To further validate its capability to capture water-insoluble membrane antigens, purified cell membranes were co-incubated with MnBP@pGluCP. The resulting protein profiles were remarkably similar to those of purified cancer cell membranes (Figure S9a, Supporting Information). These findings strongly suggest that MnBP@pGluCP can efficiently and simultaneously capture both water-soluble and water-insoluble tumor cell membrane antigens. This superior antigen-capturing ability enhances antigenic diversity, providing a broader range of antigenic peptides for T cell recognition, and promoting a more comprehensive immune response. Coupled with its exceptional capture of water-insoluble membrane antigens, this approach improves the diversity and efficiency of antigen presentation, thereby laying a solid experimental foundation for the antigen-capture mechanism proposed herein.

To verify whether MnBP@pGluCP can indeed simultaneously capture water-soluble and water-insoluble tumor cell membrane antigens to mimic pathogen-like particles and enhance antigen presentation efficiency, bone marrow-derived DCs (BMDCs) were co-incubated with the antigenic nanocomplexes. As shown in Figure 3e,f, MnBP had some stimulatory capacity for BMDCs compared to controls, as MnBP was limited in the amount and type of antigen capture, and DC maturation was more predominantly due to the successful activation of the STING pathway. In contrast, MnBP@pGluCP, which can adsorb both water-insoluble and water-soluble antigens, was more effective in enhancing the antigen presentation efficiency of BMDCs and could promote high expression levels of maturation markers, such as CD80 and CD86, which enhanced the immune response. The expression of BMDC surface markers after capturing different types of antigens was further investigated. As expected, the MnBP@pGluCP nanocomplexes that captured both water-insoluble and water-soluble antigens exhibited the highest levels of SIINFEKL peptides compared to the adsorption of either water-soluble or water-insoluble membrane antigens alone (Figure S9b,c, Supporting Information), confirming their significantly improved cross-presentation efficiency. More importantly, the nanocomplexes capturing multiple types of antigens outperformed the single-antigen nanocomplexes in simultaneously inducing DC maturation and enhancing antigen-presenting ability (Figure S9b,d,e, Supporting Information). These results suggest that the antigenic MnBP@pGluCP complexes are effective in stimulating DC maturation and cross-presentation due to the activation of the STING pathway by Mn^{2+} in the complex and the capture of a high number and abundance of antigens.

2.6. In Vitro Cell Uptake Study

The capture of antigens by APCs, such as DCs, is a critical step in eliciting an effective immune response.[34] Capitalizing on the distinctive cell membrane adhesion properties of pGluCP, the endocytosis of MnBP@pGluCP in DCs was investigated. Ovalbumin (OVA), labeled with Cy5.5, served as a model antigen to simulate tumor antigen proteins. DC2.4 cells were incubated with Cy5.5-labeled MnBP@pGluCP (MnBP@pGluCP/OVA-Cy5.5) or MnBP (MnBP/OVA-Cy5.5) for 4 h. Confocal laser scanning microscopy (CLSM) images, in conjunction with Pearson's correlation coefficients analysis for colocalization, revealed that MnBP/OVA-Cy5.5 nanoparticles could attach to the cell membrane. However, the pGluCP-modified MnBP/OVA-Cy5.5 nanoparticles adhered to the cell surface in significantly greater quantities (**Figure 4a**; Figure S10a,b, Supporting Information). Over time, the number of MnBP@pGluCP/OVA-Cy5.5 nanoparticles bound to the cell surface progressively increased (Figure 4b,c; Figure S10c, Supporting Information), suggesting that the interaction between pGluCP and phosphatidylcholine on the DC cell membrane substantially enhances antigen adherence to the DC surface, facilitating antigen uptake by DCs.

Further examination of antigen uptake by DCs was conducted. Flow cytometry analysis demonstrated that only 21.8% of MnBP was endocytosed by DCs, whereas the endocytosis

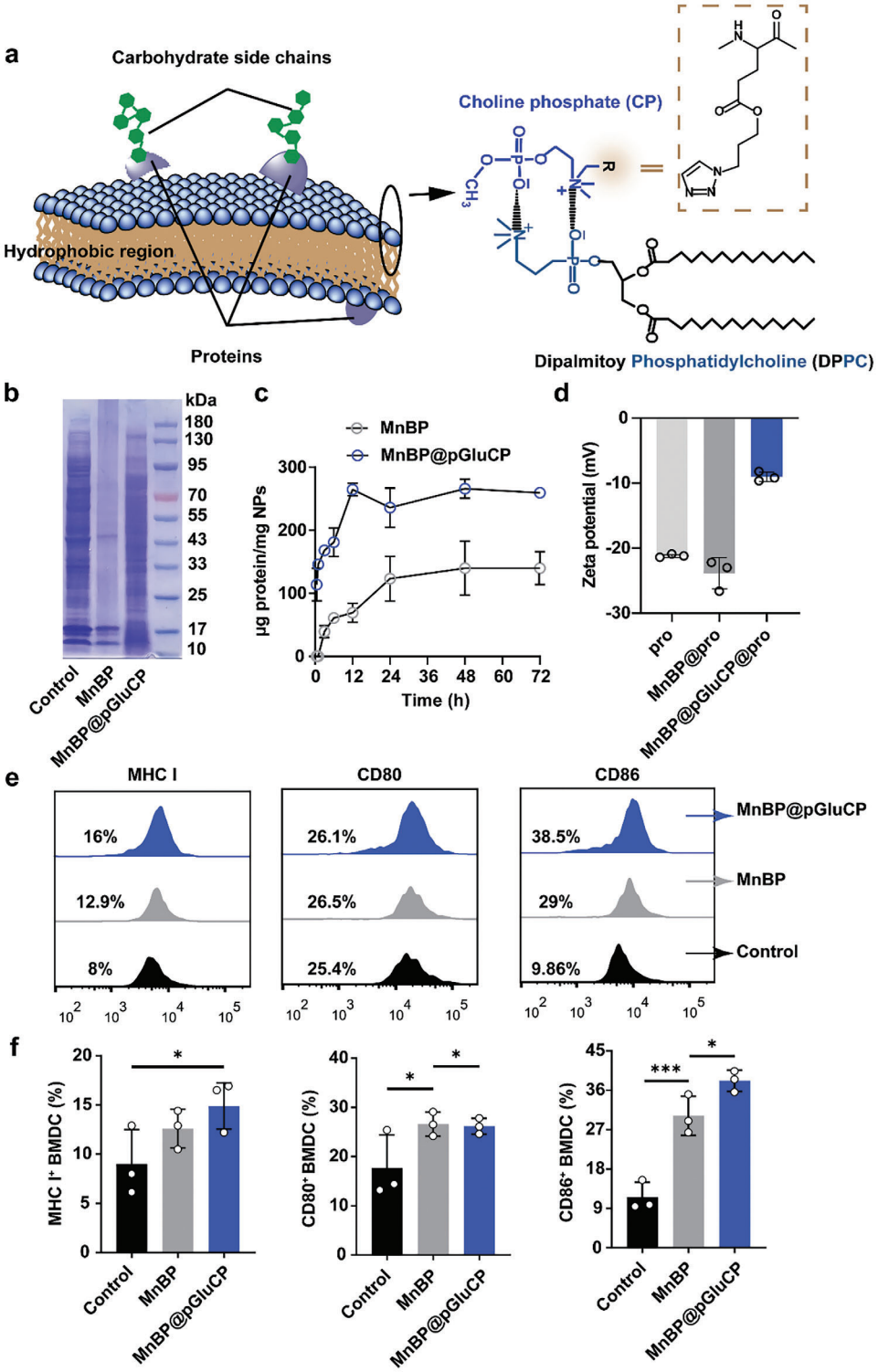

Figure 3. Simultaneous capture of water-soluble and water-insoluble tumor antigens by MnBP@pGluCP nanocomplex enhances cross-presentation efficiency. a) Schematic diagram of the structure of the cell membrane. b) SDS-PAGE protein analysis of 4T1 cell lysates, MnBP and MnBP@pGluCP. c) Amount of protein captured by different nanoparticles after co-incubation with supernatant. d) Changes of zeta potential of the MnBP or MnBP@pGluCP after incubation with 4T1 cell lysate. e) Representative flow cytometry plots of MHC I, CD80, and CD86 expression on BMDCs. f) Quantitative analysis of MHC I, CD80, and CD86 expression levels on BMDCs. All data are presented as mean ± SD ($n = 3$). *$p < 0.05$, and ***$p < 0.001$.

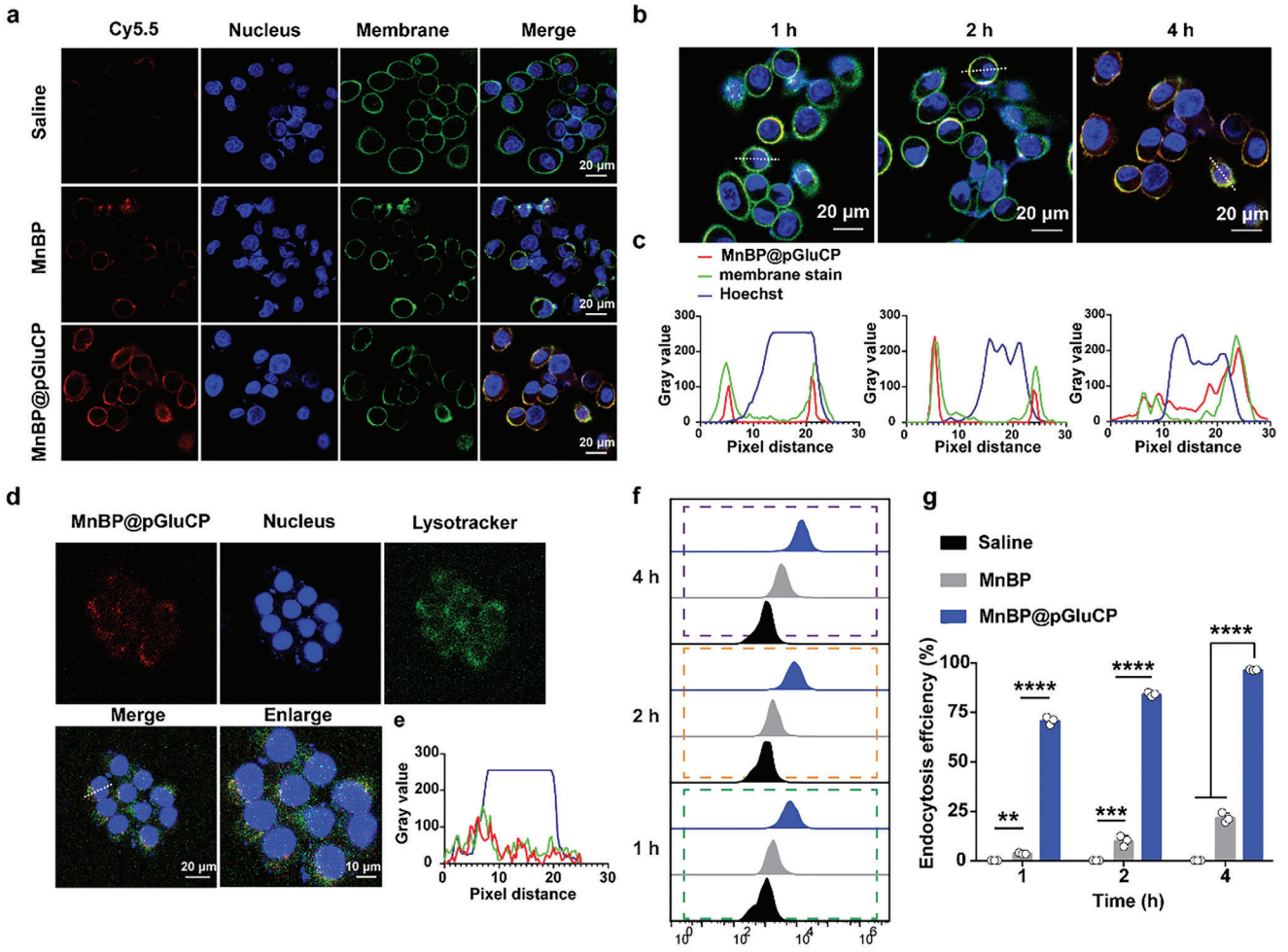

Figure 4. Evaluation of the cellular uptake. a) Confocal images of DCs after incubation with MnBP, MnBP@pGluCP for 4 h. Nucleus and membrane were stained by Hoechst 33 342 (blue) and CellMask Deep Red (red), respectively. b) Confocal laser scanning microscopy images of cellular uptake of MnBP@pGluCP-Cy5.5 by the DC cells after 1, 2, or 4 h of incubation. c) Spatial-intensity profiles of MnBP@pGluCP in DC cells at 1, 2, or 4 h respectively. d) Subcellular location of MnBP@pGluCP (red) in DC cells. The lysosome was stained by lysotracker (green) and the nucleus was stained by ADPI. e) Spatial-intensity profiles of MnBP@pGluCP in DC cells. f) Flow cytometric and quantitative analysis g) of internalization of MnBP@pGluCP-Cy5.5 by the DC cells after 1, 2, or 4 h of incubation at 37 °C. All data are presented as mean ± SD ($n = 3$). $^{**}p < 0.01$, $^{***}p < 0.001$, and $^{****}p < 0.0001$.

ratio for MnBP@pGluCP under identical conditions reached a remarkable 96.5% (Figure 4f,g; Figure S9d,e, Supporting Information). To verify the cytoplasmic delivery of MnBP@pGluCP, lysosomes were stained using LysoTracker Green and then co-incubated with MnBP@pGluCP for 6 h. The red fluorescence and green fluorescence were observed at the same time under CLSM, demonstrating the co-localization between MnBP@pGluCP (red) and lysosomes (green) (Figure 4d). These observations collectively suggest that pGluCP-modified nanoparticles not only augment the internalization of antigens but also enable the co-delivery of antigens and adjuvants to APCs, thereby enhancing the immune response.

In summary, the combination of efficient antigen capture and enhanced cell uptake by APCs, facilitated by the pGluCP modification of MnBP, positions MnBP@pGluCP as a promising candidate for the development of advanced vaccine platforms aimed at boosting the immune response against cancer. The synergy between antigen capture and antigen presentation, driven by the unique properties of MnBP@pGluCP, holds significant potential for advancing cancer immunotherapy strategies.

2.7. In Vitro BMDCs Maturation Evaluation

The preceding findings suggest that MnBP, under NIR laser irradiation, generates tumor antigens that are subsequently captured by the pGluCP polymer-modified MnBP, culminating in the formation of an in situ tumor nanovaccine enriched with antigens and adjuvants. Intrigued by this, the effect of the in situ nanovaccines on DC activation in vitro was further investigated on the BMDCs and the secretion of inflammatory cytokines in different treatment groups. PBS was set as the negative control. The expression of MHC I, MHC II, CD80, and CD86 on BMDCs in the MnBP@pGluCP group was significantly higher than those in the other groups, attributing to its high efficiency in capturing antigens released from ICD (**Figure** 5a–f; Figure S11,

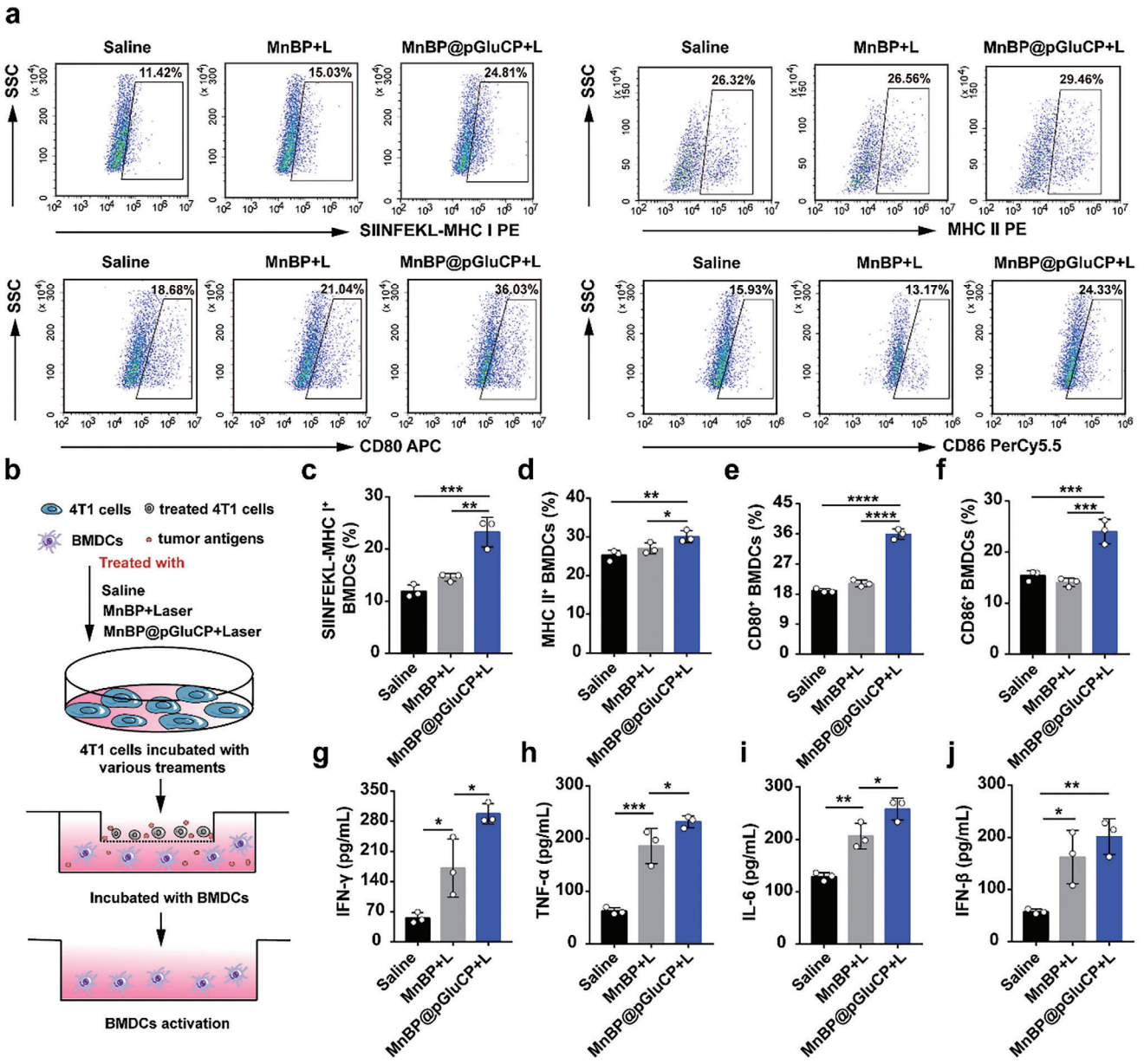

Figure 5. Immune activation of BMDCs. a) Representative flow cytometry data and statistic data to show the expression of SIINFEKL-MHC I, MHC II, CD80, and CD86 after the different treatments in vitro. b) Schematic illustration of the Transwell coculture system for DC activation in vitro. The expression of SIINFEKL-MHC I c), MHC II d), CD80 e), and CD86 f) in the BMDC cell culture supernatant after different treatments. The secretion of IFN-γ g), TNF-α (h), IL-6 i), and IFN-β j) were further checked by ELISA. All data are presented as mean ± SD ($n = 3$). *$p < 0.05$, **$p < 0.01$, ***$p < 0.001$, and ****$p < 0.0001$.

Supporting Information). This enhancement was attributed to the superior antigen-capturing efficiency of MnBP@pGluCP from ICD-derived antigens.

Moreover, the antigen-captured MnBP@pGluCP (MnBP@pGluCP@antigen) showed an augmented secretion of interferon-gamma (IFN-γ), tumor necrosis factor-alpha (TNF-α), and interleukin-6 (IL-6), underscoring its ability to effectively activate DCs and promote antigen cross-presentation (Figure 5g–i). Encouraged by the efficient cytoplasmic delivery of MnBP@pGluCP and the release of intracellular Mn^{2+}, IFN-β (a type I IFN that has been shown to induce a robust $CD8^+$ T-cell response and is an important indicator of successful activation of the STING pathway[35,36]) was measured by ELISA. The findings suggested that MnBP and MnBP@pGluCP significantly promoted the expression of IFN-β, suggesting that they could effectively activate the STING pathway (Figure 5j). These findings collectively highlight the dual role of MnBP@pGluCP in capturing tumor antigens released by ICD and facilitating DC activation alongside the captured antigens. Additionally, Mn^{2+} was found to effectively activate the STING pathway,

exerting adjuvant-like effects. Together, these effects promote DC activation and antigen presentation.

2.8. Accumulation and PTT Effects of MnBP@pGluCP at the Tumor Sites

To ensure an effective anti-tumor effect in vivo, it is important to explore the retention of nanoparticles at the injection site. To study the retention of the material at the tumor site, the OVA-Cy5.5 assembled materials were randomly injected in situ into the tumor site when the 4T1 tumors reached 50 mm^3 in mice, and fluorescence imaging was performed at 1, 2, 4, 8, 10, 12, 24, 36, and 48 h after administration (Figure S12a,b, Supporting Information). MnBP and MnBP@pGluCP could be retained at the tumor site, with a slow decrease in fluorescence with time. Meanwhile, tumors were collected for ex vivo fluorescence imaging after 48 h. Compared to MnBP, MnBP@pGluCP achieved better tumor accumulation ability (Figure S12c, Supporting Information), attributed to the cell membrane adhesion of pGluCP. This membrane adhesion prolongs antigen retention at the tumor site to generate a sustained and strong anti-tumor immune response.

Based on the superior in vitro photothermal effect of MnBP, in vivo photothermal imaging was performed on tumor-bearing mice after injection of saline, MnBP, and MnBP@pGluCP. The mice treated with MnBP and MnBP@pGluCP experienced a notable elevation in body temperature (Figure S13, Supporting Information), attesting to the potential of MnBP-containing materials for photothermal therapy in vivo. Crucially, localized gentle heating facilitates the recruitment of diverse immune cells, including DCs and effector T cells, thereby unveiling a plethora of TAAs, setting the stage for a coordinated immune assault on the tumor. These findings underscore the multifaceted role of MnBP@pGluCP in orchestrating an effective anti-tumor response, from antigen capture and DC activation to tumor accumulation and photothermal therapy, positioning it as a promising candidate for cancer immunotherapy.

2.9. In Vivo Immunogenic Effect Evaluation in Primary 4T1 Tumors

Given the clinical significance of αPD-1, an immune checkpoint blockade antibody that modulates T cell activity, αPD-1 was incorporated into the in situ vaccine strategy. Specifically, αPD-1 reverses immune tolerance in $CD8^+$ T cells in 4T1 tumors by interacting with PD-1 receptors, thereby refining the vaccine approach. Following the establishment of 4T1 tumors on the right flank of mice, mice were randomly assigned to one of five groups (n = 5) on day 7 post-inoculation: 1) PBS, 2) MnBP+L, 3) MnBP@pGluCP+L, 4) MnBP@pGluCP-αPD-1, or 5) MnBP@pGluCP-αPD-1+L. To validate the successful assembly of the in situ vaccine and its impact on DAMP release, we observed a marked expression of CRT at the tumor site in the groups co-treated with NIR (**Figure 6a**), indicative of successful vaccine assembly. To assess the tumor-specific immunotoxicity of our engineered in situ vaccine, splenocytes from immunized mice subjected to various treatments were co-cultured with 4T1 tumor cells in vitro (Figure 6b). After 24 h of incubation, a significant number of splenocytes from the MnBP@pGluCP+L and MnBP@pGluCP-αPD-1+L groups were observed to adhere to 4T1 cells (Figure 6c). The survival of tumor cells was further quantified using a CCK-8 assay. As depicted in Figure 6d, the MnBP@pGluCP+L group exhibited higher tumor-killing efficiency compared to the MnBP+L group. However, the group treated with MnBP@pGluCP-αPD-1+L displayed the strongest cytotoxic effect against 4T1 cells, with an efficiency reaching ≈70%, providing compelling evidence for antigen-specific CTL responses.

The immunological cascade encompasses tumor antigen release, antigen presentation, and T-cell activation and infiltration.[37] Successful release and capture of TAAs have been demonstrated. Next, the antigen-presenting capacity of DCs in spleens was evaluated. The results represented that the percentage of $CD11c^+MHC\ I^+$ of splenocytes was obviously increased in the MnBP@pGluCP-αPD-1+L group compared with the saline group (Figure S14a–c, Supporting Information). A similar trend was assessed for the proportion of $CD11c^+MHC\ II^+$ of splenocytes (Figure S14b,d, Supporting Information). These findings suggest that MnBP@pGluCP-αPD-1+L significantly enhanced antigen presentation, thereby facilitating the subsequent activation of the immune system. Furthermore, to confirm the immune activation capacity, mature DCs are considered as important competent APCs for modulating adaptive immunity and thus cross-priming effector T cells.[38] Therefore, the results of flow cytometry assay showed that the proportion of mature DCs ($CD11c^+CD80^+$, $CD11c^+CD86^+$) in spleens was significantly increased in the MnBP@pGluCP+L and MnBP@pGluCP-αPD-1+L group as compared to the saline and MnBP+L groups, attributing to the massive killing of tumor cells and release of a large amount of tumor-associated antigens by MnBP in response to the laser. At the same time, the antigens release and the enhanced antigen capture by pGluCP (Figure S14e,f, Supporting Information) enhanced antigen presentation. Additionally, MnBP+L demonstrated stronger DC activation than the saline group, likely due to the stimulation of immune cell activation by Mn^{2+} through the activation of the STING pathway, exerting an adjuvant-like effect, and the local photothermal effect. Conversely, the reduced efficacy of MnBP@pGluCP-αPD-1 was attributed to insufficient availability of tumor antigens for effective vaccine action.

Subsequently, the proportion of $CD8^+$ T cells in the immune organs was detected (Figure S15, Supporting Information). As shown in Figure 6f, the percentage of $CD8^+$ effector T cells in splenocytes was notably higher in the MnBP@pGluCP-αPD-1+L group compared to other groups, reflecting the antigen-capturing capability of pGluCP and the regulation of PD-1. Both the MnBP@pGluCP+L and MnBP@pGluCP-αPD-1+L groups significantly increased the proportion of $CD3^+$ $CD8^+$ T cells in LNs compared to the saline or MnBP+L groups (Figure 6g). Consistently, the size of the inguinal LNs was significantly larger in the MnBP@pGluCP+L and MnBP@pGluCP-αPD-1+L groups, indicating a robust immune response in the lymph nodes (Figure S16, Supporting Information). Moreover, expression levels of IFN-γ, TNF-α, and IL-6 cytokines, which are essential indicators of anti-tumor immune responses, were measured in restimulated splenocytes by ELISA. As shown in Figure 6h, cytokine levels in the MnBP@pGluCP+L group were higher than

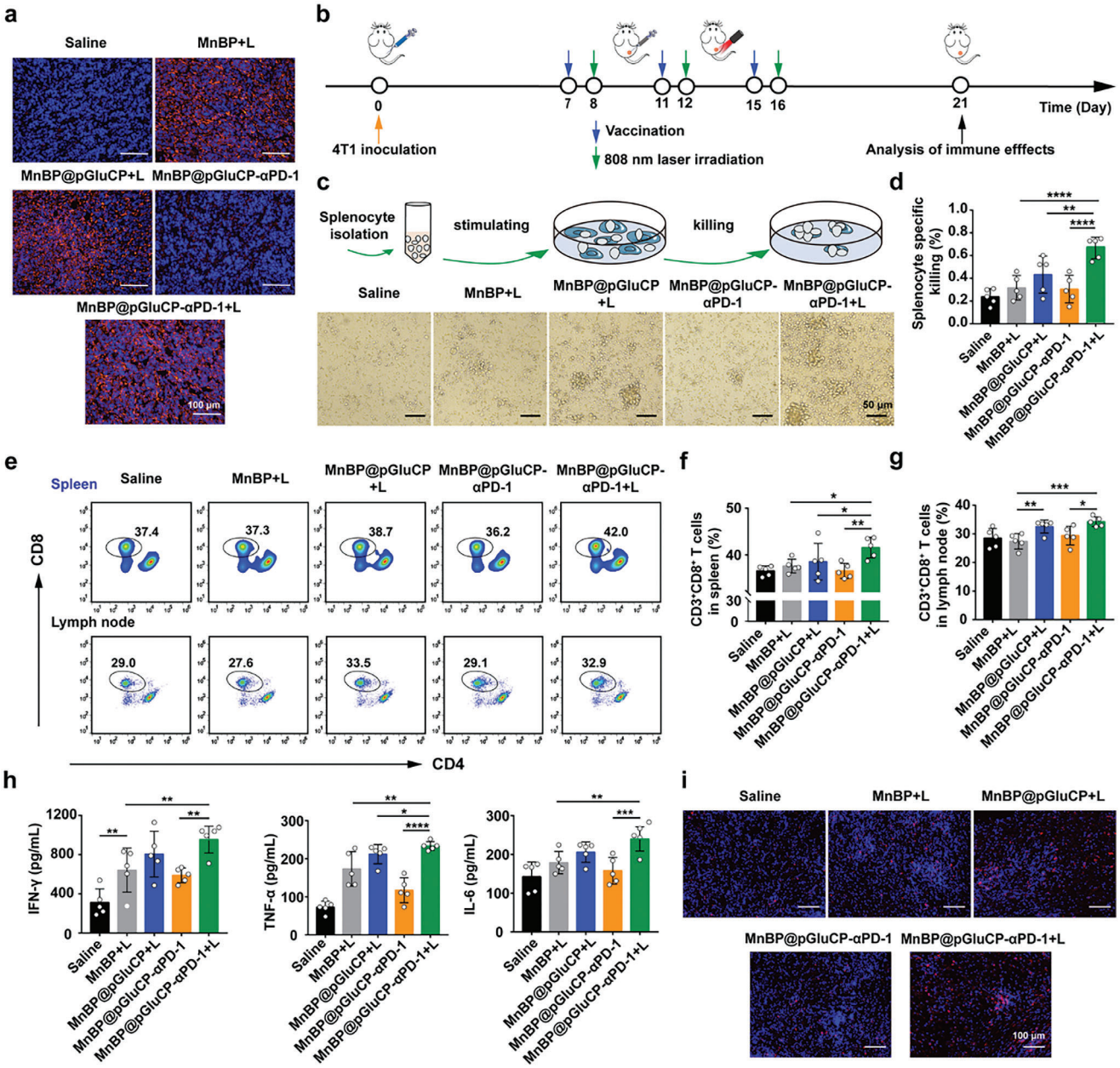

Figure 6. Antitumor immunity study in a unilateral 4T1 tumor model. a) Immunofluorescence staining of CRT of tumor sites after various treatments. Scale bar = 100 μm. b) Scheme of the tumor challenge experiment in the primary tumor model. c) Schematic illustration and photographs of tumor cell-specific killing studies. d) Quantitative data showing the specific killing ability of splenocytes from various treatment mice. e) Flow cytometric analysis of CD4/CD8$^+$ T cells in spleens. f) The proportion of CD3$^+$CD8$^+$ T cells in spleens from the mice. g) The proportion of CD3$^+$CD8$^+$ T cells in lymph nodes from mice. h) Secreted levels of IFN-γ, TNF-α, and IL-6 were measured by ELISA. i) Immunofluorescence staining of CD8$^+$ T cells in the tumors. Scale bar = 100 μm. All data are presented as mean ± SD ($n = 5$). *$p < 0.05$, **$p < 0.01$, ***$p < 0.001$, and ****$p < 0.0001$.

those in the MnBP+L group, suggesting that the antigen-capture nanoplatform-based PTT elicited a robust in vivo anti-tumor immune response and could generate a potent immune response to antigen restimulation. The MnBP@pGluCP-αPD-1+L group had the highest cytokine levels, benefiting from the synergistic effect of PTT combined with the immune checkpoint blockade strategy.

Immunofluorescence staining further confirmed the infiltration of T lymphocytes. As illustrated in Figure 6i, a greater distribution of CD8$^+$ T cells was observed in tumors treated with MnBP@pGluCP-αPD-1+L. In addition, there were no significant changes in mouse body weight during the treatment period (Figure S17, Supporting Information). Biochemical indices of mice, including alanine aminotransferase (ALT), aspartate aminotransferase (AST), blood urea nitrogen (BUN), and creatinine (CREA), remained within normal ranges (Figure S18a, Supporting Information), and no obvious change could be observed in all treatment groups (Figure S18b, Supporting Information),

indicating the negligible side effects and good tolerance of mice during antitumor therapy. Overall, the MnBP@pGluCP+L group not only triggered a pronounced immune response in the spleen and LNs but also efficiently generated antigen-specific CTLs, highlighting its potential as a powerful strategy for cancer immunotherapy. The integration of αPD-1 further amplified the immunogenic effects, underscoring the therapeutic benefits of combining photothermal therapy with immune checkpoint blockade in enhancing antitumor immunity.

2.10. In Vivo Vaccine Efficacy on the Bilateral 4T1 Tumor Model

Motivated by the above results of remarkable anti-tumor effect and potent immune activation efficacy in unilateral tumor-bearing mice treated with PTT, we next investigated the inhibition of the constructed in situ tumor vaccine on distal tumors using a bilateral 4T1 tumor model, as schemed in **Figure** 7a.

The primary tumor used for vaccine construction was meticulously monitored for volume changes throughout three inoculation periods. As displayed in Figure 7b, both the MnBP+L and MnBP@pGluCP+L groups exhibited antitumor effects; however, the antitumor efficacy of the MnBP@pGluCP-αPD-1+L group was the most pronounced, underscoring the enhancement conferred by the introduction of αPD-1 in suppressing both primary and distal tumor growth. Moreover, the volume changes in distal tumors without laser irradiation were also tracked, revealing that the combination of local photothermal therapy, antigen capture, and immune checkpoint blockade resulted in the most potent antitumor efficacy in distal tumors (Figure 7c). No significant change was observed in the body weight of mice in different groups, suggesting the low systemic toxicity of these nanosheets (Figure 7d). Photographs of primary isolated tumors and the corresponding weights showed that the groups with laser irradiation showed better tumor suppression than the group without irradiation (Figure 7e). The photographs and weights of tumors isolated from distal tumors showed that the laser irradiation group produced stronger anti-tumor immune responses, significantly inhibiting the growth distal of tumor as compared to the group without laser irradiation, in which the distal tumors of some mice in the MnBP@pGluCP+L and MnBP@pGluCP-αPD-1+L group were completely inhibited, and the tumor growth in the MnBP@pGluCP-αPD-1+L group was inhibited to the greatest extent (Figure 7f). Hematoxylin and eosin (H&E) staining of primary (upper) and distal (bottom) tumor tissues showed extensive necrosis in primary and distal 4T1 tumors treated with MnBP@pGluCP+L and MnBP@pGluCP-αPD-1+L, and only part of tumor cells was killed in the MnBP+L group, whereas the tumor cells in saline and MnBP@pGluCP-αPD-1 groups were more viable (Figure 7g).

DCs capturing antigens can migrate to LNs near the tumor and become activated, the maturation status of DCs in the tumor-draining LNs (TDLNs) was evaluated using flow cytometry. The results showed that in the LNs on the side of the primary tumor side, the level of mature DCs ($CD11c^+CD80^+CD86^+$) in the group of MnBP@pGluCP-αPD-1+L was presented up to 23%, and significantly increased compared to other groups. While the levels of mature DCs were only 16.1%, 19.0%, and 15.7% in the case of saline, MnBP+L, and MnBP@pGluCP-αPD-1 group, respectively (**Figure** 8a,b; Figure S19, Supporting Information). Moreover, the percentage of $CD8^+$ T cells in TDLNs from the MnBP@pGluCP+L group exceeded that of the saline group by 10% (Figure 8d,e; Figure S20, Supporting Information).

The results of the flow cytometry assay of the lymphocytes on the distal tumor side depicted in Figure 8c,f, the proportions of the mature DCs and $CD8^+$ T cells in TDLNs from the MnBP@pGluCP-αPD-1+L group were both obviously higher than the groups without laser irradiation. Interestingly, the MnBP@pGluCP+L group demonstrated higher proportions of DC maturation and $CD8^+$ T cell presence in LNs proximal to both primary and distal tumors compared to the MnBP+L group. This could be attributed to the efficient uptake of soluble and insoluble antigens by MnBP@pGluCP, which enhanced the vaccine's chassis action and created a rich intracellular vaccine repertoire for sustained vaccine construction. This is critical because prolonged and sustained vaccine exposure to immune cells enhances and prolongs adaptive immunity. A similar trend was observed for $CD8^+$ T cell infiltration in the spleens (Figure S21, Supporting Information). In addition, infiltration of $CD8^+$ T cells of tumors (left and right) was detected by the flow cytometry and immunofluorescence staining. Compared to groups without laser irradiation, a significant increase in the proportion of $CD8^+$ T cell infiltration was detected in tumors on both sides in the MnBP@pGluCP-αPD-1+L group (Figure 8g–i), indicating the systemic antitumor immune responses effectively induced by the in situ vaccine constructed by MnBP@pGluCP-αPD-1+L. This is critical for inhibiting tumor recurrence and metastasis.

TDLNs were collected from mice that had undergone various treatments. The volume of LNs was notably increased in mice treated with MnBP@pGluCP-αPD-1+L bearing 4T1 tumors (Figure S22, Supporting Information), affirming the strong immune response triggered by the in situ vaccine constructed from MnBP@pGluCP-αPD-1+L. Moreover, H&E staining of the hearts, livers, spleens, lungs, and kidneys of mice did not reveal significant histopathological changes (Figure S23, Supporting Information), underscoring the excellent biocompatibility of these formulations. These results demonstrate that these formulations have good biocompatibility. In conclusion, this in situ nanovaccine system, capable of generating antigens, capturing antigens, and integrating with adjuvants in situ, can effectively augment T-cell immunity and prevent the growth of both primary and distal tumors. Additionally, by binding to anti-PD-1 monoclonal antibodies, it induces T-cell-mediated anti-tumor immune responses, positioning it as a promising strategy for cancer immunotherapy.

3. Conclusion

In situ tumor vaccines represent a transformative approach in cancer therapy, distinguished by their inherent advantages of bypassing the complexities of antigen identification, expediting drug development timelines, and addressing tumor heterogeneity. Central to the efficacy of such vaccines is the critical initial step of antigen delivery by APCs, which often serves as the rate-limiting factor in the ensuing vaccine-induced immune cascade. In this pioneering study, we unveil an innovative in situ photothermal vaccine (MnBP@pGluCP-αPD-1), meticulously designed to harness the synergistic power of mild photothermal

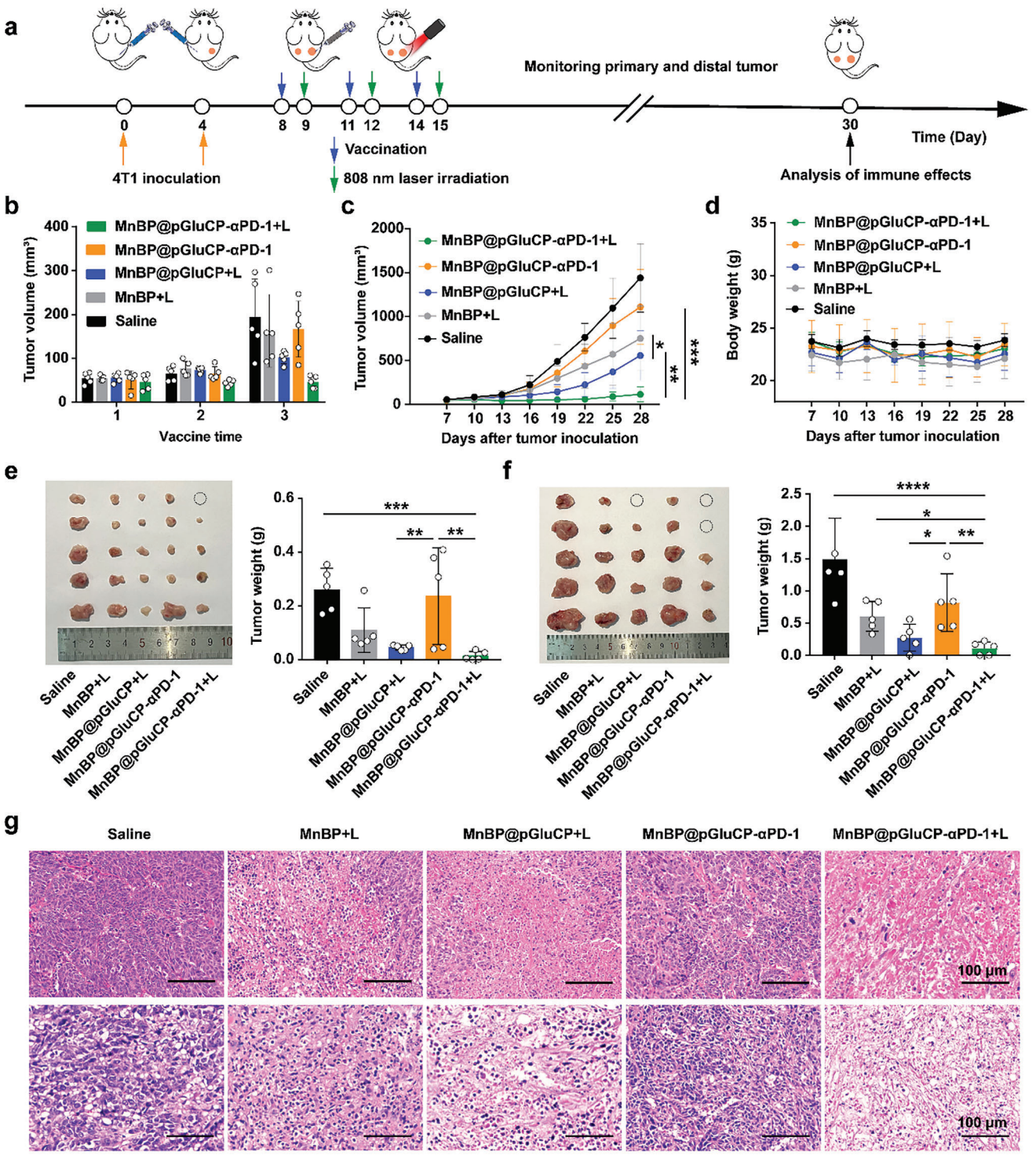

Figure 7. Antitumor immunity study in a bilateral 4T1 tumor model. a) Schematic illustration of the in vivo treatment schedule. b) Volume of tumor in situ during inoculation. c) Average tumor growth curves of the distal 4T1 tumor. d) Body weight changes of mice in different groups. e) Photograph and the weight of primary tumors. f) Photographs and the weight of distal tumors. g) Representative H&E-stained images of 4T1 tumors after different treatments. Scale bar = 100 μm. All data are expressed as mean ± SD ($n = 5$). *$p < 0.05$, **$p < 0.01$, ***$p < 0.001$, and ****$p < 0.0001$.

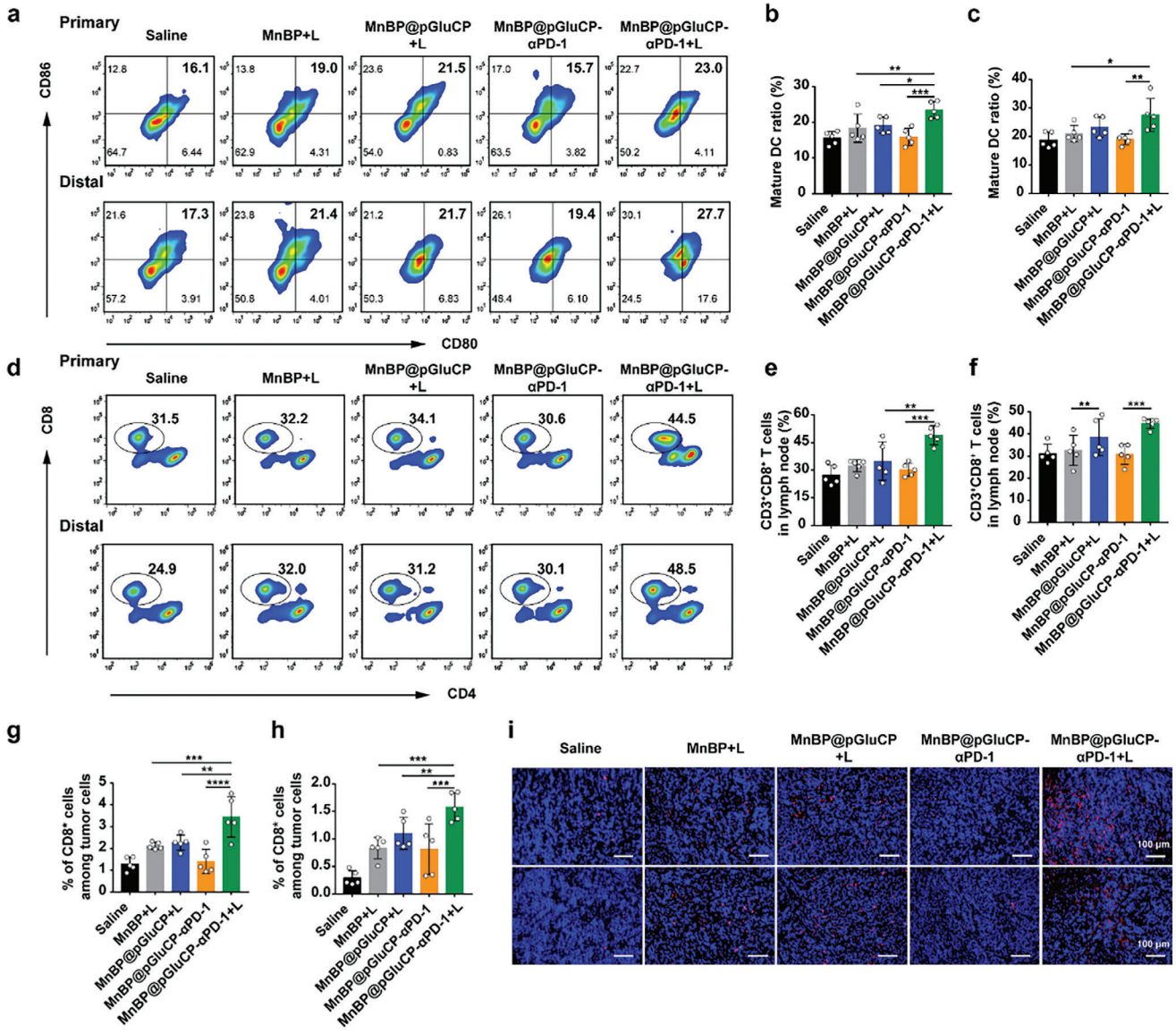

Figure 8. In situ tumor vaccination had a systemic antitumor effect. a) Representative flow cytometry images of DCs and the percentage of the matured DCs in LNs in primary b) and distal c) tumor side after various treatments. d) Representative flow cytometry images and the percentage of $CD8^+$ T cells in primary e) and distal f) tumors after various treatments. g) The percentage of $CD8^+$ T cells in primary and distal tumors h) after various treatments. i) Immunofluorescence staining of $CD8^+$ T cells in the tumors. All data are presented as mean ± SD ($n = 5$). *$p < 0.05$, **$p < 0.01$, ***$p < 0.001$, and ****$p < 0.0001$.

therapy, superior antigen capture capabilities, and the modulation of the immunosuppressive tumor microenvironment. This vaccine leverages pGluCP, a macromolecule endowed with exceptional antigen-capturing and cell-membrane-adhesion properties, to amplify the antigen-presenting efficiency of APCs. The key multiple mechanism underpinning the effectiveness of our vaccine formulation is the dual impact of PTT-induced ICD effects and the activation of the STING pathway by Mn^{2+} ions, and the simultaneous capture of multiple quantities and abundances of antigens, which collectively bolster the maturation of DCs. Moreover, the strategic integration of PD-L1 checkpoint blockade immunotherapy into our vaccine design further amplifies its anti-tumor efficacy, showcasing superior outcomes in inhibiting both primary and distant tumor growth. This combination therapy not only fortifies the immune system's ability to recognize and destroy cancer cells but also overcomes the barriers posed by the immunosuppressive TME, thereby enhancing overall treatment efficacy.

4. Experimental Section

Materials and Reagents: The bulk BP crystals were purchased from Mophos (China) and stored in a dark Ar glove box. N-methy-2-lpyrrolidone (NMP, 99.5%), anhydrous ethanol (analytical, >99.9%), and aqua ammonia were purchased from Sigma (Thermo Fisher Scientific, USA).

$MnCl_2{\cdot}H_2O$ was bought from Macklin (Shanghai, China). The Annexin V-FITC/PI apoptosis detection kit and RIPA lysis buffer were purchased from Keygen Bio TECH (Nanjing, China). CCK-8 assay, red blood cell lysis buffer, and DAPI were purchased from Beyotime (Shanghai, China). Cell culture medium RPMI 1640, fetal bovine serum, and penicillin-streptomycin were purchased from Gibco (CA, USA). Hoechst 33342, Cell Mask Green Plasma Membrane Stain, and Lysotracker Green DND-26 were purchased from ThermoFisher Scientific (Waltham, USA). FITC-TUNEL cell apoptosis detection kit and CD8-GB13429 were purchased from Servicebio (Wuhan, China). Flow cytometry antibody dyes and cytokine ELISA kits were obtained from BioLegend (CA, USA). LumiKineTM Xpress mIFN-β 2.0 ELISA kit was purchased from InvivoGen (San Diego, CA, USA). Mouse GM-CSF and mouse IL-4 were purchased from PeproTech (NJ, USA). Anti-TBK1 antibody and anti-Phospho-TBK1 antibody were purchased from Biodragon (Suzhou, China). Anti-STING antibody and anti-Phospho-STING antibody were obtained from Immunoway (Texas, USA). Anti-Histone H3.1 antibody and the goat anti-rabbit/mouse HRP-conjugated secondary antibody were obtained from Abmart (Shanghai, China). Female BALB/c and C57BL/6 mice (4–6 weeks) were provided by Beijing HFK Laboratory Animal Technology Co., Ltd. (Beijing, China). In addition, the cells used in this article were purchased from Guangzhou First Military Hospital (Guangzhou, China). All animal experiments were conducted following animal ethics and approved by the Ethics Committee of Jinan University.

Preparation of BP, MnBP, and MnBP@pGluCP Nanosheets—Preparation of Bare BP Nanosheets: The preparation of bare BP nanosheets was achieved through a solvent exfoliation technique. Specifically, 20 mg of BP was dispersed in 20 mL of NMP and subjected to ultrasonication in an ice bath for an extended period of 18 h at a power output of 600 W. This rigorous sonication facilitated the exfoliation of the bulk material into nanoscale sheets. Subsequently, the resultant suspension underwent centrifugation at a high speed of 12 000 rpm for 10 min. This step was crucial for the removal of any larger, unexfoliated particles, ensuring the homogeneity and desired size range of the nanosheet dispersion. The supernatant, now enriched with the exfoliated BP nanosheets, was carefully collected and preserved for subsequent use in further experiments or modifications. This meticulous preparation method yields high-quality BP nanosheets, suitable for a variety of advanced applications requiring their unique properties.

Preparation of BP, MnBP, and MnBP@pGluCP Nanosheets—Preparation of MnBP Nanosheets: The preparation of MnBP was executed through an in situ deposition methodology. Initially, a 10 mL suspension of BP in NMP at a concentration of 50 μg mL^{-1} was prepared. This suspension was then mixed with 0.1% (v/v) ammonia (1.0 M) under gentle stirring conditions (100 rpm) at 40 °C for a duration of 2 h. This step was critical for priming the BP surface for the subsequent mineralization process. Following the surface conditioning phase, an aqueous solution of $MnCl_2$ at 90 mM (1 mL) was carefully introduced to the suspension. The reaction mixture was allowed to equilibrate at room temperature for 12 h with continuous stirring at 300 rpm in a controlled dark environment. This extended reaction period facilitated the in situ deposition of manganese phosphate onto the BP nanosheets, leading to the formation of MnBP nanosheets. Post-reaction, the product was subjected to centrifugation to isolate the synthesized MnBP nanosheets. The precipitate was thoroughly rinsed with ethanol and distilled water to eliminate any unreacted ionic species, ensuring the purity of the MnBP nanosheets.

Preparation of BP, MnBP, and MnBP@pGluCP Nanosheets—Preparation of MnBP@pGluCP Nanosheets: The preparation of MnBP@pGluCP nanosheets involved the charge interaction between negatively charged MnBP nanosheets and positively charged pGluCP. Briefly, the MnBP suspension was mixed with varying concentrations of pGluCP solutions (MnBP: pGluCP mass ratios of 1: 6, 1: 12, and 1: 24) at room temperature for 2 h. The mixture was centrifuged at 10 000 rpm for 5 min, followed by the removal of the supernatant and collection of the precipitate. The resultant MnBP@pGluCP nanosheets were freeze-dried and stored at 4 °C for subsequent use.

Preparation of BP, MnBP, and MnBP@pGluCP Nanosheets—Preparation of MnBP@pGluCP-αPD-1: The conjugation of αPD-1 to MnBP@pGluCP was achieved by adding a concentrated αPD-1 solution dropwise into the MnBP@pGluCP suspension under stirring conditions at 4 °C for 4 h. The crude MnBP@pGluCP-αPD-1 complex was then purified via high-speed centrifugation (12 000 rpm, 10 min) to remove excess αPD-1. The purified MnBP@pGluCP-αPD-1 complex was subsequently freeze-dried and stored for future use.

Characterizations: Transmission electron microscopy (TEM) images were captured by Transmission electron microscopy (JEM-2010-HR, Japan), high-resolution TEM (HRTEM), and energy dispersive X-ray spectroscopy (EDS) were performed on the JEOL JEM-2100F at 200 kV. The hydrodynamic diameters of nanomaterials were performed by the Zetasizer Nano ZS (Malvern, UK). The UV–vis absorption spectra of the samples were measured by a UV–vis spectrophotometer (UV–vis, Shimadzu UV-2550, Japan). The infrared absorption spectra were measured using a Fourier transform infrared (FT-IR) spectrophotometer (Vertex 70, Bruker, Germany). FT-IR measurements were performed using the KBr pressing method in the region of 4000–400 cm^{-1} with a resolution of 4 cm^{-1}. Powder X-ray diffraction pattern (XRD, D8 advance, Bruker, German) was obtained from 10° to 70° with Cu-Kα ($\lambda = 1.54056$ Å) radiation. X-ray photoelectron spectroscopy (XPS) measurement was analyzed on Thermo Fisher ESCALAB 250 Xi XPS. ^1H NMR and ^{13}C NMR spectra were measured on a Bruker AV-400 spectrometer with D_2O as a single solvent.

Photothermal Performance Assessment of MnBP: The photothermal conversion efficiency of MnBP was systematically investigated under various conditions. First, the influence of laser power density on temperature elevation was assessed using a 100 μg mL^{-1} MnBP suspension, exposed to NIR laser irradiation at intensities of 0.5, 0.8, 1.0, and 1.5 W cm^{-2}. Subsequently, the photothermal heating curves were generated by monitoring the temperature changes of MnBP suspensions at different concentrations (20, 40, 60, 80, 100 μg mL^{-1}) under a constant laser power density of 1.5 W cm^{-2}. The temperature variations were recorded at regular intervals using an infrared thermal camera (FOTRIC, Shanghai, China). Comparative studies were also conducted on MnBP and MnBP@pGluCP suspensions at concentrations of 60, 80, and 100 μg mL^{-1} under identical irradiation conditions. Water served as the negative control throughout these experiments.

In Vivo Photothermal Effect Evaluation: In vivo photothermal effect of MnBP and MnBP@pGluCP was evaluated in the 4T1 tumor model. 4T1 cells (5×10^5/mouse) were inoculated in the right flank of the mice, and when the tumor reached 50 mm^3, the tumor was irradiated at 1.5 W cm^{-2} after in situ injection of MnBP or MnBP@pGluCP, and photographed with the infrared thermal camera at 0, 1, and 3 min, respectively.

In Vivo Accumulation Analysis: The prepared MnBP or MnBP@pGluCP were mixed with Cy5.5 to obtain MnBP-Cy5.5 and MnBP@pGluCP-Cy5.5 for in vivo imaging. 4T1 cells (1×10^6/mouse) were subcutaneously injected into the right flank of mice, when the tumor volumes reached ≈50 mm^3, MnBP-Cy5.5 or MnBP@pGluCP-Cy5.5 was injected randomly into the 4T1-tumor-bearing mice, the mice were imaged at different time intervals. The mice were euthanized at the last time point and tumors were isolated for ex vivo imaging. Fluorescence intensity was analyzed by Living Imaging Software.

Cell Apoptosis Assay: Cell apoptosis was quantitatively determined by a flow cytometer (Beckman Coulter, USA) using Annexin V-FITC/PI dual staining following the manufacturer's instructions. The 4T1 cells (2×10^5 cells per well) were seeded on six-well plates and treated with MnBPs or MnBP@pGluCP for 12 h. At the 6th h after irradiation, the cells were processed by washing with pre-cooled PBS and collected after trypsinizing. After centrifuging (1500 rpm, 5 min), the supernatant was discarded, and the cells were re-suspended in pre-cooled 1×Binding Buffer, and then stained with the Annexin V-FITC/PI. All samples were incubated at room temperature and protected from light for 3 min. Finally, the apoptotic cells were quantified by the flow cytometer and analyzed using the FlowJo software.

ICD Investigation: The ICD triggered by MnBP and MnBP@pGluCP was assessed through the detection of CRT exposure, HMGB1 release, and ATP production. 4T1 cells (1×10^5 cells per well) were seeded into six-well plates and incubated overnight. Cells were then treated with MnBP or MnBP@pGluCP (100 μg mL^{-1}) or saline (as a control), followed by laser irradiation for 3 min. Extracellular supernatants were collected to quantify

HMGB1 and CRT secretion using ELISA kits, while ATP production was measured using an ATP assay kit.

Determination of Intracellular Manganese Content: DC2.4 cells were seeded into a six-well plate and incubated overnight. Afterward, the medium was replaced with fresh media containing MnBP or MnBP@pGluCP (100 μg mL^{-1}). After 24 h of incubation, the cell suspensions were collected after trypsinizing, quickly frozen, slowly thawed, and centrifuged. The supernatant was collected to detect intracellular manganese content by using an ICP-MS (Thermo iCAP 7000 AERIES, USA).

Western Blotting Analysis: To detect the activation of the STING pathway, DC2.4 cells were harvested and lysed with RIPA buffer containing protease and phosphatase inhibitors. The lysates were centrifuged, and the supernatants were collected as total protein extracts. Equal amounts of protein (30 μg) were separated by 10% SDS-PAGE and transferred to a PVDF membrane. The membrane was blocked with rapid protein sealing solution, incubated with primary antibodies overnight at 4 °C, followed by HRP-conjugated secondary antibodies for 1 h at room temperature. Protein bands were visualized using an ECL substrate and analyzed with ImageJ software.

Assessment of Simultaneous Antigen Capture and Presentation: To assess the simultaneous capture of water-soluble and water-insoluble tumor membrane antigens and their impact on antigen presentation, the following protocol was employed. Briefly, 4T1 cells were lysed using RIPA buffer containing protease and phosphatase inhibitors. The lysate was centrifuged at 12 000 rpm for 10 min at 4 °C. The supernatant, containing water-soluble proteins, was collected. The pellet, containing the cellular debris and water-insoluble membrane components, was resuspended in PBS. MnBP or MnBP@pGluCP was added to both the supernatant and the resuspended pellet to capture the antigens. The mixture was incubated for 1 h at room temperature with gentle agitation. For the supernatant, the pGluCP-antigen complexes were collected by centrifugation. For the resuspended pellet, the pGluCP-coated membrane antigens were allowed to settle by gravity. The captured antigens were washed with PBS and then used for downstream analysis.

For quantitative analysis, the total protein amounts were analyzed by BCA assay kit. The potential changes of the antigen-nanocomplexes were measured by DLS. Meanwhile, the antigen-nanocomplexes were also subjected to SDS-PAGE to evaluate the purity and integrity of the captured antigens. Subsequently, the antigen-nanocomplexes were used to activate BMDCs. BMDCs were incubated with the antigen-nanocomplexes for a specified period. The activation status of the BMDCs was assessed using the flow cytometry to analyze the expression levels of maturation markers such as MHC I, CD80, and CD86.

In Vitro Cell Uptake Study: First, the prepared MnBP or MnBP@pGluCP were mixed with Cy5.5 to obtain MnBP-Cy5.5 and MnBP@pGluCP-Cy5.5. Subsequently, DC2.4 cells were seeded into a 15 mm Petri dish at a density of 1×10^4 cells and incubated overnight. Then, the culture medium was replaced with fresh media containing MnBP-Cy5.5 or MnBP@pGluCP-Cy5.5 (100 μg mL^{-1}), and the cells were continuously cultured for 1, 2, or 4 h, respectively. Thereafter, the cells were stained with Hoechst 33 342 (10 mmol L^{-1}) and Cell Mask Green (5 μg mL^{-1}) for 15 min. The cells were then observed under a confocal laser scanning microscope (CLSM, Zeiss, LSM 880). The results were analyzed using ZEN software. Furthermore, DC2.4 cells were cultured with MnBP-Cy5.5 or MnBP@pGluCP-Cy5.5 (100 μg mL^{-1}) for 24 h at 37 °C. Subsequently, cells were stained with Lyso-Tracker Green DND-26 for 2 h to identify lysosomes, followed by fixation with 4% paraformaldehyde for 20 min. Nuclei were counterstained with DAPI for 5 min before observation under the CLSM. The flow cytometry was also utilized to quantitatively determine the uptake efficiency of the nanosheets.

In Vitro BMDC Activation: To study the activation of BMDCs, a transwell system was employed. 4T1 cells were cultured in the upper chamber of the transwell system, while BMDCs were seeded in the lower chamber. 4T1 cells were initially co-cultured with saline, MnBP, or MnBP@pGluCP for 6 h. Following this, cells were either irradiated with an 808 nm laser (1.5 W cm^{-2}, 3 min) or left untreated. After 24 h post-irradiation, BMDCs were harvested from the lower chamber, stained with antibodies against CD11c-FITC, SIINFKEL MHC I-PE, MHC II-PE, CD80-APC, and CD86-PerCy5.5, and analyzed by the flow cytometry to evaluate their activation status. Additionally, the levels of secreted cytokines including IFN-γ, TNF-α, IL-6, and IFN-β in the cell culture supernatants were quantified using ELISA kits.

Vaccine Efficacy Assessment on a Unilateral Tumor Model: In a strategic investigation, BALB/c mice were subcutaneously inoculated with 4T1 cells (5×10^5 cells per mouse) on the right flank. Once the tumors reached ≈50 mm^3, the mice were divided into five groups:1) saline, 2) MnBP+L, 3) MnBP@pGluCP+L, 4) MnBP@pGluCP-αPD-1, and 5) MnBP@pGluCP-αPD-1+L. Herein, the concentration of formulations was 100 μg mL^{-1}. The groups with NIR laser irradiation were treated with 808 nm laser at the power of 1.5 W cm^{-2} for 3 min after administration. The mice were euthanized when the tumor volume reached 1000 mm^3. On day 21, critical biological specimens including tumors, spleens, LNs, and blood were meticulously collected for comprehensive analysis.

Tumors were processed for immunofluorescence analysis targeting CRT and $CD8^+$ T cells to elucidate the immune microenvironment. Spleens were harvested to isolate splenocytes, enabling the assessment of DC maturation and antigen-presenting capabilities in vivo. Splenocytes were stained with a panel of antibodies including anti-CD11c-FITC, anti-SIINFKEL MHC I-PE, anti-MHC II-PE, anti-CD80-APC, and anti-CD86-PerCy5.5. Further, T-cell differentiation was quantified through staining with anti-APC-CD3, anti-FITC-CD4, and anti-PerCy5.5-CD8 antibodies. The cytotoxic effect of splenocytes from vaccinated mice on 4T1 tumor cells was also evaluated. The ratio of $CD3^+CD8^+$ T cells in LNs was quantified using flow cytometry. ELISA assays were employed to measure cytokine levels (IFN-γ, TNF-α, and IL-6) from restimulated splenocytes.

To investigate the pathological changes in the main organs of the mice after receiving different treatments, the mice were euthanized and the main organs including the heart, liver, spleen, lung, and kidney were collected, fixed with 4% paraformaldehyde and stained with H&E for histopathology assessment. Meanwhile, blood was collected from mice at the end of the treatment for long-term toxicity evaluation. The following indicators were tested: AST, ALT, BUN, and CREA.

Vaccine Efficacy on a Bilateral Tumor Model: To probe the vaccine's systemic impact on distant tumors, a bilateral tumor model was established. Mice received subcutaneous injections of 4T1 cells (5×10^5 cells per mouse) on both the right (primary tumor) and left (distal tumor) flanks, with the latter inoculation occurring four days later. Upon reaching a size of ≈50 mm^3, the primary tumor was subjected to the same treatment regimens as in the unilateral model, while the distal tumor remained untreated. Tumor dimensions were measured biweekly using vernier calipers, and volumes were calculated using the formula $V = 1/2a^2 \times b$, where "a" is the shorter and "b" is the longer diameter. Body weight measurements were also taken biweekly. Finally, the mice were euthanized, and their spleens, inguinal LNs, and tumors were excised for further analysis.

Immunofluorescence staining was utilized to determine the $CD8^+$ T cell ratio in tumors. Splenocytes were again isolated, stained, and analyzed to evaluate DC maturation and T-cell differentiation. Organs from each group were harvested for immunohistochemical analysis, providing insights into tissue-specific immune responses and potential adverse effects.

Statistical Analysis: The GraphPad Prism 9.5 Software was used to perform the statistical analysis. The results were expressed as means ± standard deviation (SD). Statistical analysis was analyzed using an unpaired Student's *t*-test (two-tailed) for two groups, and a one-way analysis of variance (ANOVA) for multiple comparisons. Significance levels were defined as $*p < 0.05$, $**p < 0.01$, $***p < 0.001$, and $****p < 0.0001$.

Supporting Information

Supporting Information is available from the Wiley Online Library or from the author.

Acknowledgements

This work was financially supported by the Science and Technology Program of Guangzhou, China (No. 202103030004), National Natural Sci-

ence Foundation of China (No.82374306), Natural Science Foundation of Hunan Province (No.2023JJ30456), Guangdong Basic and Applied Basic Research Foundation (2023A1515011221).

Conflict of Interest

The authors declare no conflict of interest.

Data Availability Statement

The data that support the findings of this study are available from the corresponding author upon reasonable request.

Keywords

antigen capture, antigen presentation, in situ tumor vaccines

Received: September 11, 2024
Revised: December 20, 2024
Published online:

[1] H. H. Hussey, *JAMA* **1974**, *227*, 435.
[2] I. Mellman, G. Coukos, G. Dranoff, *Nature* **2011**, *480*, 480.
[3] L. Hammerich, A. Binder, J. D. Brody, *Mol. Oncol.* **2015**, *9*, 1966.
[4] A. Marabelle, L. Tselikas, T. de Baere, R. Houot, *Ann. Oncol.* **2017**, *28*, xii33.
[5] L. Li, J. Zou, Y. Dai, W. Fan, G. Niu, Z. Yang, X. Chen, *Nat. Biomed. Eng.* **2020**, *4*, 1102.
[6] Y. Li, K. Zhang, Y. Wu, Y. Yue, K. Cheng, Q. Feng, X. Ma, J. Liang, N. Ma, G. Liu, G. Nie, L. Ren, X. Zhao, *Small* **2022**, *18*, 2107461.
[7] V. Sunil, A. Mozhi, W. Zhan, J. H. Teoh, C.-H. Wang, *Biomaterials* **2021**, *275*, 120974.
[8] Y. Zhang, S. Ma, X. Liu, Y. Xu, J. Zhao, X. Si, H. Li, Z. Huang, Z. Wang, Z. Tang, W. Song, X. Chen, *Adv. Mater.* **2021**, *33*, 2007293.
[9] H. Zhang, Y. Zhang, H. Hu, W. Yang, X. Xia, L. Lei, R. Lin, J. Li, Y. Li, H. Gao, *Small* **2023**, *19*, 2301041.
[10] X. Li, X. Cai, Z. Zhang, Y. Ding, R. Ma, F. Huang, Y. Liu, J. Liu, L. Shi, *Nano Lett.* **2020**, *20*, 4454.
[11] L. Jin, D. Yang, Y. Song, D. Li, W. Xu, Y. Zhu, C.-F. Xu, Y. Lu, X. Yang, *ACS Nano* **2022**, *16*, 15226.
[12] M. Fan, L. Jia, M. Pang, X. Yang, Y. Yang, S. Kamel Elyzayati, Y. Liao, H. Wang, Y. Zhu, Q. Wang, *Adv. Funct. Mater.* **2021**, *31*, 2010587.
[13] B. N. Yalamandala, T. M. H. Huynh, M.-R. Chiang, W.-H. Weng, C.-W. Chang, W.-H. Chiang, S.-H. Hu, *Adv. Funct. Mater.* **2023**, *33*, 2210644.
[14] Z. R. Dong, W. J. Liu, K. H. Liu, Y. Lu, W. Wu, J. P. Qi, Z. J. Chen, *Drug Discovery Today* **2021**, *26*, 1712.
[15] X. F. Yu, Z. H. Liu, J. Janzen, I. Chafeeva, S. Horte, W. Chen, R. K. Kainthan, J. N. Kizhakkedathu, D. E. Brooks, *Nat. Mater.* **2012**, *11*, 468.
[16] X. Yu, Y. Zou, S. Horte, J. Janzen, J. N. Kizhakkedathu, D. E. Brooks, *Biomacromolecules* **2013**, *14*, 2611.
[17] X. Yu, X. Yang, S. Horte, J. N. Kizhakkedathu, D. E. Brooks, *Macromol. Biosci.* **2014**, *14*, 334.
[18] W.-l. Wang, X.-j. Ma, X.-f. Yu, *Chin. J. Polym. Sci.* **2017**, *35*, 1352.
[19] W. Wang, S. Jiang, S. Li, X. Yan, S. Liu, X. Mao, X. Yu, *Chem. Mater.* **2021**, *33*, 774.
[20] W. Wang, B. Wang, S. Liu, X. Shang, X. Yan, Z. Liu, X. Ma, X. Yu, *ACS Appl. Mater. Interfaces* **2017**, *9*, 15986.
[21] X. Yu, X. Yang, S. Horte, J. N. Kizhakkedathu, D. E. Brooks, *Chem. Commun.* **2013**, *49*, 6831.
[22] W. Wang, B. Wang, X. Ma, S. Liu, X. Shang, X. Yu, *Biomacromolecules* **2016**, *17*, 2223.
[23] X. Yu, X. Yang, S. Horte, J. N. Kizhakkedathu, D. E. Brooks, *Biomaterials* **2014**, *35*, 278.
[24] S. Li, X. Xie, W. Wang, S. Jiang, W. Mei, Y. Zhang, S. Liu, X. Yu, *Nanoscale* **2022**, *14*, 2277.
[25] Z. Guo, S. Li, Y. Qu, J. Lu, W. Xue, X. Yu, Z. Liu, *Chem. Eng. J.* **2021**, *417*, 127970.
[26] T. Pan, W. Fu, H. Xin, S. Geng, Z. Li, H. Cui, Y. Zhang, P. K. Chu, W. Zhou, X.-F. Yu, *Adv. Funct. Mater.* **2020**, *30*, 2003069.
[27] P.-M. Chen, W.-Y. Pan, C.-Y. Wu, C.-Y. Yeh, C. Korupalli, P.-K. Luo, C.-J. Chou, W.-T. Chia, H.-W. Sung, *Biomaterials* **2020**, *230*, 119629.
[28] X. Yang, Y. Yang, J. Bian, J. Wei, Z. Wang, Z. Zhou, Z. Li, M. Sun, *Nano Today* **2021**, *38*, 101109.
[29] D. Huang, T. Wu, S. Lan, C. Liu, Z. Guo, W. Zhang, *Biomaterials* **2022**, *289*, 121808.
[30] M. Wang, J. Song, F. F. Zhou, A. R. Hoover, C. Murray, B. Q. Zhou, L. Wang, J. L. Qu, W. R. Chen, *Adv. Sci.* **2019**, *6*, 1802157.
[31] J. Yang, M. Hou, W. Sun, Q. Wu, J. Xu, L. Xiong, Y. Chai, Y. Liu, M. Yu, H. Wang, Z. P. Xu, X. Liang, C. Zhang, *Adv. Sci.* **2020**, *7*, 2001088.
[32] L. Apetoh, F. Ghiringhelli, L. Zitvogel, *M S-Med. Sci.* **2007**, *23*, 257.
[33] L. Apetoh, F. Ghiringhelli, A. Tesniere, M. Obeid, C. Ortiz, A. Criollo, G. Mignot, M. C. Maiuri, E. Ullrich, P. Saulnier, H. Yang, S. Amigorena, B. Ryffel, F. J. Barrat, P. Saftig, F. Levi, R. Lidereau, C. Nogues, J. P. Mira, A. Chompret, V. Joulin, F. Clavel-Chapelon, J. Bourhis, F. André, S. Delaloge, T. Tursz, G. Kroemer, L. Zitvogel, *Nat. Med.* **2007**, *13*, 1050.
[34] S. C. Eisenbarth, *Nat. Rev. Immunol.* **2019**, *19*, 89.
[35] C. Y. Chen, Y. H. Tong, Y. S. Zheng, Y. J. Shi, Z. W. Chen, J. Li, X. L. Liu, D. Zhang, H. H. Yang, *Small* **2021**, *17*, 2006970.
[36] T. Song, Y. Liao, Q. Zuo, N. Liu, Z. Liu, *J. Mater. Chem. B* **2022**, *10*, 3474.
[37] D. S. Chen, I. Mellman, *Immunity* **2013**, *39*, 1.
[38] M. Collin, N. McGovern, M. Haniffa, *Immunology* **2013**, *140*, 22.